Design of Cerenkov Radiation–Assisted Photoactivation of TiO$_2$ Nanoparticles and Reactive Oxygen Species Generation for Cancer Treatment

Shalinee Kavadiya and Pratim Biswas

Aerosol and Air Quality Research Laboratory, Center of Aerosol Science and Engineering, Department of Energy, Environmental and Chemical Engineering, Washington University, St. Louis, Missouri

The use of Cerenkov radiation to activate nanoparticles in situ was recently shown to control cancerous tumor growth. Although the methodology has been demonstrated to work, to better understand the mechanistic steps, we developed a mathematic model that integrates Cerenkov physics, light interaction with matter, and photocatalytic reaction engineering. **Methods:** The model describes a detailed pathway for localized reactive oxygen species (ROS) generation from the Cerenkov radiation–assisted photocatalytic activity of TiO$_2$. The model predictions were verified by comparison to experimental reports in the literature. The model was then used to investigate the effects of various parameters—the size of TiO$_2$ nanoparticles, the concentration of TiO$_2$ nanoparticles, and the activity of the radionuclide ^{18}F-FDG—on the number of photons and ROS generation. **Results:** The importance of nanoparticle size in ROS generation for cancerous tumor growth control was elucidated, and an optimal size was proposed. **Conclusion:** The model described here can be used for other radionuclides and nanoparticles and can provide guidance on the concentration and size of TiO$_2$ nanoparticles and the radionuclide activity needed for efficient cancer therapy.

Key Words: cancer treatment; Cerenkov radiation; nuclear decay; photocatalysis; photodynamic therapy

Radionuclides are being used for various medical applications, from imaging for disease diagnosis to therapy. Therapeutic uses include tumor growth control for cancer, in which the high-intensity radiation from the nuclide kills cancer cells. In a recent development, another exciting property of radionuclides—the production of Cerenkov radiation (CR)—was used for imaging (*1–6*). CR is electromagnetic radiation produced when a charged particle travels in a medium at a speed exceeding that of light in that medium (*7*). The fast-moving charged ion polarizes the medium along its direction of movement, resulting in the small displacement of electrons. When the electrons relax, spheric waveforms generated along the ion track interfere constructively at a specific angle to the direction of movement and produce electromagnetic radiation (*8,9*). CR has a broadband emission in which the intensity decreases with increasing wavelength. Moreover, the radiation is generated locally within a given tissue, improving the signal-to-noise ratio for imaging applications. However, CR produces a low light intensity; thus, detecting the signal is often challenging. To overcome this issue, varieties of fluorophores, such as small molecules (*10*), quantum dots (*11,12*), and nanoparticles (*13*), are used to convert Cerenkov light into long-wavelength radiation.

Recently, CR was also used as a light source for chemical and therapeutic applications (*14–16*). In 2015, Kotagiri et al. (*15*) demonstrated the use of CR generated by the ^{18}F-FDG radionuclide to activate TiO$_2$ nanoparticles in vivo to produce reactive oxygen species (ROS) and suppress the growth of cancer cells. Since then, there has been growing interest in CR-assisted photodynamic therapy (PDT). TiO$_2$ is a known photocatalyst for energy (*17–20*) and environmental (*21,22*) applications. It has a band gap of 3.2 eV and absorbs UV light efficiently—properties that match the high-intensity regimen of CR. Kamkaew et al. (*16*) reported a system with a ^{89}Zr radionuclide (Cerenkov radiation source) and chlorin e6 (photocatalyst) and demonstrated its advantage in ROS generation through CR. Two radionuclides—^{68}Ga and ^{18}F—were recently studied for their cellular uptake and effectiveness in cancer treatment (*23,24*).

Although there has been experimental validation of local generation of ROS in the vicinity of tumors using CR (*25*), there is a need for a mechanistic understanding to better optimize the process and expand clinical deployment. In this regard, it is crucial to establish a quantitative correlation between the CR-produced light signal and the amount of ROS generation. In previous works, the CR yield of various radionuclides was modeled using the Frank–Tamm equation and Monte Carlo simulation (*26–30*). However, there has been no work on modeling the efficiency of CR activation of TiO$_2$ nanoparticles and the corresponding amount of ROS generation. The photoactivity of TiO$_2$ nanoparticles and the subsequent reaction for ROS generation have been studied—but primarily under activation by an external constant light source (*21,31*). However, systems containing time-dependent light sources distributed around TiO$_2$ nanoparticles, such as CR generated from distributed radionuclides, are more complex and have not been explored.

We have developed a mathematic model that integrates Cerenkov physics, light extinction, and photocatalytic reaction engineering to identify the mechanistic steps involved in cancer cell destruction in the presence of radionuclides and semiconducting TiO$_2$ nanoparticles. First, we calculated the amount of CR generated by the ^{18}F-FDG radionuclide. Second, we determined the light radiation absorbed

by TiO₂ nanoparticles. Finally, we calculated the amount of ROS (hydroxyl and superoxide) generated with time. The model predictions were validated with experimental results from the literature. Additionally, we studied the effects of parameters, such as the radioactivity of ¹⁸F-FDG and the concentration and size of TiO₂ nanoparticles, on the amount of ROS. With the help of this model, the doses of radionuclides and TiO₂ nanoparticles of a particular size needed to suppress cancer cell growth can be optimized.

MATERIALS AND METHODS

Figure 1 shows a schematic description of PDT. The system consists of an ¹⁸F-FDG radionuclide (CR source), TiO₂ nanoparticles (CR absorber), and cancer cells in a biologic fluid. The model primarily accounts for cell death by ROS generated from the activation of a photocatalyst by CR. Other mechanisms due to the radionuclide–nanoparticle interaction, such as ionization and excitation of the nanoparticle by ionizing radiation, are not considered. The effects of these mechanisms on the model are described later in this article. Moreover, the radiolysis of water is negligible with the used radioactivity value (32). Different parts of the integrated model are described next.

Cerenkov Physics

The number of TiO₂ nanoparticles (N_{TiO_2}, number/cm³) is calculated from the concentration (C_{TiO_2}, mol/L) and the size of the TiO₂ nanoparticles as

$$N_{TiO_2} = \frac{C_{TiO_2}}{\rho_{TiO_2} v_p}, \qquad \text{Eq. 1}$$

where ρ_{TiO_2} is the density and v_p is the volume of 1 TiO₂ nanoparticle of diameter d_p. ¹⁸F decays to stable ¹⁸O nuclei and releases 1 β-particle with a 97% probability, considered to be the source of CR. The number of subatomic β-particles (N_β) generated per second is related to the radioactivity of the ¹⁸F-FDG radionuclide (A, Bq), which decreases with time (half-life of ¹⁸F, 109.7 min):

$$N_\beta = A. \qquad \text{Eq. 2}$$

TiO₂ nanoparticles and ¹⁸F-FDG molecules are considered uniformly dispersed, and the average distance (x_{avg}) between the point of generation of β-particles and TiO₂ is determined by

$$x_{avg} = \left(\frac{1}{N_{TiO_2} + N_\beta}\right)^{1/3}. \qquad \text{Eq. 3}$$

If the β-particle travels in the medium faster than the speed of light, it generates CR. The number of Cerenkov photons generated from a β-particle per second is described by Frank–Tamm equations (33):

$$\frac{d^2 N_{ph}}{dld\lambda} = 2\pi\alpha\left(1 - \frac{1}{\beta^2 n^2}\right)\frac{1}{\lambda^2}, \quad \beta n > 1, \qquad \text{Eq. 4a}$$

$$\cos\theta = 1/\beta n, \qquad \text{Eq. 4b}$$

and

$$\beta = \left(1 - \frac{(m_o c^2)^2}{(E + m_o c^2)^2}\right)^{1/2}. \qquad \text{Eq. 4c}$$

Here, N_{ph} is the number of Cerenkov photons per second, l is the β-particle path length, α is a structure constant (1/137), β is the ratio of the velocity of charged particles to the velocity of light in a vacuum (v_p/c), n is the refractive index of the medium (assumed constant), λ is the wavelength, m_o is the rest mass of the β-particle, and E is the energy of the β-particle. The Cerenkov photons originating from a β-particle move at an angle θ from the trajectory of the β-particle.

The number of photons is calculated at each step along the β-particle trajectory. As the β-particle travels, the loss in its energy is determined from the range–energy relationship (34), and the energy is updated at every step in its path. Because all of the β-particles have different initial energies and follow an energy spectrum, Equation 4a (for N_{ph}) is weighted by the relative probability of a β-particle of a given energy being emitted by the radionuclide; then the values are summed across all of the energies. The probability of each energy was taken from the β-energy spectrum available at the Lund/LBNL nuclear data search website (35). The path length (l) depends on x_{avg}, which is a function of C_{TiO_2}, A, and d_p. Therefore, N_{ph} is a function of C_{TiO_2}, A, d_p, and λ. Once the CR is generated, it travels in the system and undergoes extinction (absorption and scattering) by TiO₂ nanoparticles (explained in detail in the next paragraph). Radiation is absorbed by the TiO₂ nanoparticles, leading to the generation of electron and hole pairs (Fig. 1B). Electrons and holes react with oxygen and water molecules adsorbed on the nanoparticle surface and produce ROS, superoxide, and hydroxyl radical, respectively. ROS further attack cancer cells in the system and destroy them.

Light Extinction

To quantitatively model the photon flux to TiO₂ nanoparticles, we considered the case of 1 β-particle and 1 TiO₂ particle, in which the β-particle travels at an angle φ from the line joining the origin of the β-particle and the TiO₂ nanoparticle (Fig. 2A). The probability of a β-particle moving in the direction φ is considered in the calculation of the number of Cerenkov photons. Because Cerenkov photons in this system move at θ = 41° with respect to the β-particle, only photons generated within the l_{AB} part of the path length (Fig. 2A) will intersect with TiO₂ and be absorbed. l_{AB} and l_{OA} are given by
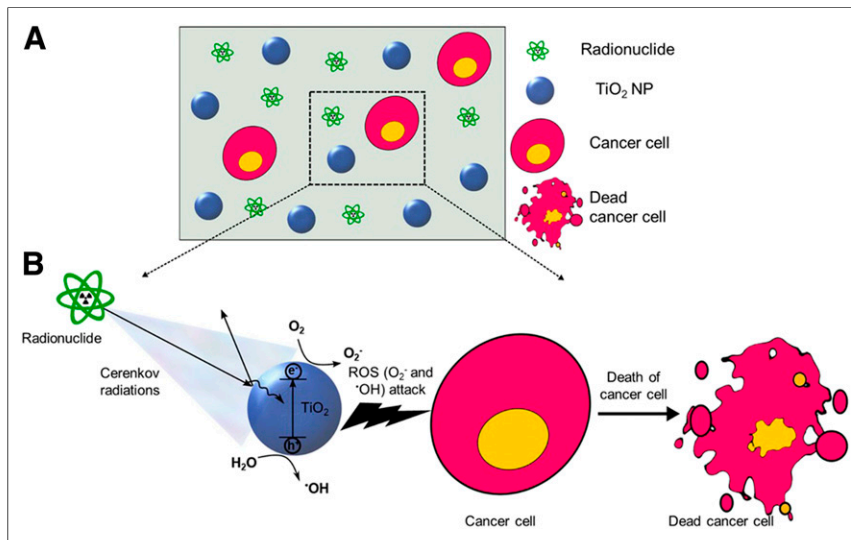

FIGURE 1. Schematic diagrams of system studied for CR-assisted PDT (A) and mechanism of ROS generation and cancer cell death from CR (B). NP = nanoparticle.
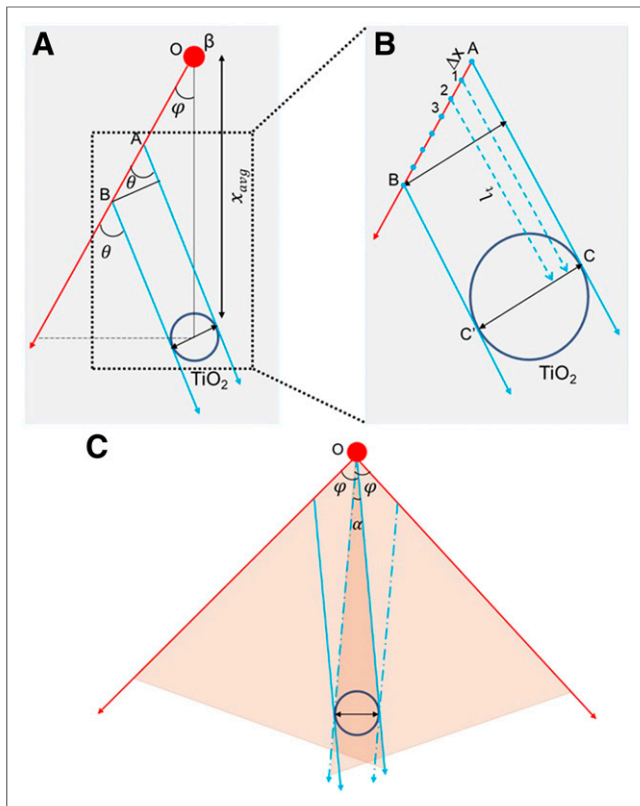
FIGURE 2. Schematic diagram depicting model. (A) β-particle (red circle) moves (red arrow) at angle to line joining origin of β and TiO₂ (hollow blue circle), and photon moves (turquoise arrows) at angle to β-trajectory. (B) l_{AB} part of β trajectory, showing that number of photons and photon flux to TiO₂ are calculated at each step with l_{AB}. (C) Angular range of interest (peach shading).

$$l_{AB} = \frac{d_p}{\sin\theta} \qquad \text{Eq. 5a}$$

and

$$l_{OA} = \frac{1}{\sin\theta}\left[(x_{avg} + R_P)\sin(\theta - \varphi) - R_P\right]. \qquad \text{Eq. 5b}$$

l_{OA} depends on x_{avg} and d_p, but l_{AB} depends only on d_p. In other words, the photons of interest are generated in a constant length segment (l_{AB}), but the location of that length segment differs for all of the β-particles, depending on their distance from TiO₂ and their trajectory (or angle φ). Once the photons are produced in the length segment l_{AB}, they travel in the medium and undergo scattering and absorption phenomena; therefore, the final number of photons reaching TiO₂ is small. The photons produced at each step travel different distances (l_t) to reach TiO₂ (Fig. 2B):

$$l_t = \left(\frac{x_{avg} + R_P}{\cos\varphi} - l_{OA} - l_{AB}\right)\frac{\cos\varphi}{\sin(\theta + \varphi)} + (l_{AB} - l)\cos\theta. \qquad \text{Eq. 6}$$

Because photons move at an angle θ with respect to the path of the β-particle, there is an angular range of φ beyond which there is no influence of the β-particle on TiO₂. In other words, Cerenkov photons do not reach TiO₂. Thus, only the β-particle moving within the angular range (Fig. 2C) will contribute to the photon flux:

$$\text{angular range} = 2\theta - \tan^{-1}\left(\frac{R_p}{R_p + x_{avg}}\right). \qquad \text{Eq. 7}$$

The photon flux (number of photons/s·cm²) reaching the TiO₂ nanoparticle is calculated at each step using Equation 8, taking into account the light extinction. Additionally, TiO₂ absorbs only below 380 nm; thus, the photon flux of interest is defined as $N_{int}(C_{TiO_2}, A, d_p, \lambda, \varphi)$, with a λ of <380 nm:

$$N_{int}\left(C_{TiO_2}, A, d_p, \lambda, \varphi\right) = \frac{N_{ph}\left(C_{TiO_2}, A, d_p, \lambda, \varphi\right)}{A_p}\exp(-bl_t). \qquad \text{Eq. 8}$$

Extinction coefficient b is:

$$b = N_{TiO_2}A_p(Q_{abs} + Q_{sca}), \qquad \text{Eq. 9a}$$

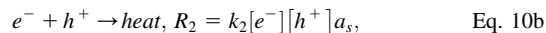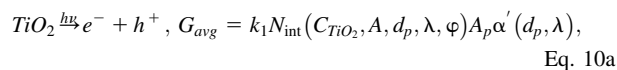$$Q_{abs} = -\frac{4\pi d_p}{\lambda}\text{Im}\left\{\frac{m^2 - 1}{m^2 + 2}\right\} = k_a d_p, \qquad \text{Eq. 9b}$$

and

$$Q_{sca} = \frac{8\pi^4 d_p^4}{3\lambda^4}\text{Re}\left\{\frac{m^2 - 1}{m^2 + 2}\right\}^2 = k_s d_p^4. \qquad \text{Eq. 9c}$$
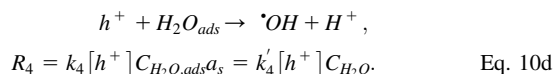
Here, Q_{abs} and Q_{sca} are the efficiencies of absorption and scattering, respectively; m is the refractive index of TiO₂ in water; and k_a and k_s are the absorption and scattering coefficients, respectively. To account for all of the β-particles, their individual contributions to N_{ph} are summed. Once the photon flux to the TiO₂ particle is obtained, the amount of ROS generation is determined.

Catalytic Reactions and ROS Production

The photocatalytic generation of free radicals is described by the following reaction mechanism (21). TiO₂ nanoparticles absorb Cerenkov photons and generate electron (e^-) and hole (h^+) pairs (Eq. 10a). There is a possibility that electrons and holes can recombine and produce heat (Eq. 10b). Alternatively, the electrons react with the oxygen molecules adsorbed on the TiO₂ surface and produce superoxide radicals (Eq. 10c), and the holes react with water molecules and produce hydroxyl radicals (Eq. 10d):

$$TiO_2 \xrightarrow{h\nu} e^- + h^+, \; G_{avg} = k_1 N_{int}\left(C_{TiO_2}, A, d_p, \lambda, \varphi\right)A_p\alpha'(d_p, \lambda),$$
$$\text{Eq. 10a}$$

$$e^- + h^+ \rightarrow heat, \; R_2 = k_2[e^-]\left[h^+\right]a_s, \qquad \text{Eq. 10b}$$

$$e^- + O_{2,ads} \rightarrow O_2^-, \; R_3 = k_3[e^-]C_{O_2,ads}a_s = k_3'[e^-]C_{O_2}, \qquad \text{Eq. 10c}$$

and

$$h^+ + H_2O_{ads} \rightarrow {}^\bullet OH + H^+,$$
$$R_4 = k_4\left[h^+\right]C_{H_2O,ads}a_s = k_4'\left[h^+\right]C_{H_2O}. \qquad \text{Eq. 10d}$$

The rate of electron–hole pair formation (Eq. 10a) depends on the photon flux and the optoelectronic properties of the TiO₂ nanoparticle. In Equations 10a–10d, $k_1 = 4.37 \times 10^{10}$ cm⁻³, $k_2 = 7.14 \times 10^6$ s⁻¹, $k_3' = k_3 K_{O_2} \approx 10^{-19}$ cm³/s, and $k_4' = k_4 K_{H_2O} = 10^{-8}$ cm³/s are the rate constants of reactions taken from the literature (36,37). K_{O_2} and K_{H_2O} are the adsorption rate constants of O₂ and H₂O, respectively. $[e^-]$ and $[h^+]$ are the electron and hole concentrations (ions per unit surface area of the TiO₂ nanoparticle), and C_{H_2O} and C_{O_2} (mM) are

the concentrations of water and dissolved oxygen, respectively. These rates are used to derive the relationships between the concentration of ROS and the various parameters (C_{TiO_2}, A, d_p, λ, and φ). The rates of formation of both radicals (superoxide and hydroxyl) are given by

$$\frac{d[O_2^-]}{dt} = k_3'[e^-]C_{O_2}a_sN_{TiO_2}, \qquad \text{Eq. 11a}$$

and

$$\frac{d[{}^\bullet OH]}{dt} = k_4'[h^+]C_{H_2O}a_sN_{TiO_2}. \qquad \text{Eq. 11b}$$

We assume that the spatial dimension of the system is large enough that any change in the concentration of water resulting from Equations 10a–10d is not significant. Simultaneously, dissolved oxygen is assumed to be available, so that C_{O_2} also remains constant. It is assumed that the adsorption equilibrium occurs instantaneously. Concentrations of electrons and holes are calculated by applying a mass balance to them:

$$\frac{d[e^-]}{dt} = G_{avg} - k_2[e^-][h^+]a_s - k_3'[e^-]C_{O_2}, \qquad \text{Eq. 12a}$$

and

$$\frac{d[h^+]}{dt} = G_{avg} - k_2[e^-][h^+]a_s - k_4'[h^+]C_{H_2O}. \qquad \text{Eq. 12b}$$

At steady state, the rate of generation of electrons (or holes) is equal to the rate of their consumption. Solving Equations 12a and 12b to derive an expression for the concentration of photogenerated electrons yields:

$$\frac{k_2k_3'}{k_4'}\frac{C_{O_2}}{C_{H_2O}}[e^-]^2 + k_3'C_{O_2}[e^-] - G_{avg} = 0, \qquad \text{Eq. 13}$$

where $G_{avg} = k_1N_{\text{int}}(C_{TiO_2}, A, d_p, \lambda, \varphi)A_p\alpha'(d_p, \lambda)$. Substituting the expression for $[e^-]$ from Equation 13 in the expression for the rate of ROS generation yields:

$$\frac{d[O_2^-]}{dt} = \frac{d[{}^\bullet OH]}{dt}$$

$$= b\left[\frac{-b \pm \sqrt{b^2 + ak_1N_{\text{int}}(C_{TiO_2}, A, d_p, \lambda, \varphi)\pi d_p^2\alpha'(d_p, \lambda)}}{2a}\right]$$

$$\times \pi d_p^2 N_{TiO_2}(C_{TiO_2}, d_p).$$

$$\text{Eq. 14}$$

In Equation 14, a and b are constants: $a = \frac{k_2k_3'}{k_4'}\frac{C_{O_2}}{C_{H_2O}}$ and $b = k_3'C_{O_2}$. Hence, the rate of ROS generation depends on d_p, C_{TiO_2}, and A. The equation is solved to determine a time variation in the ROS species concentration that can be correlated to tumor cell viability.

RESULTS

Figure 3A shows the CR spectrum, the number of Cerenkov photons/s with a radioactivity of 7.4 MBq/mL, and the concentration of 10-nm TiO$_2$ nanoparticles (2.5 µg/mL). The spectrum followed the $1/\lambda^2$ relationship with wavelength, in agreement with the Frank–Tamm equation (Eq. 4). The Cerenkov photon yield per decay from the present study was 1.38 over the wavelength range of 400–800 nm, close to the reported value of 1.3 over the same range (28).

Next we discuss the role of various system parameters in ROS generation, with the goal of determining the specifications (concentration and size) of TiO$_2$ and the radionuclide activity needed to terminate cancer cell growth.

Model Validation by Comparison to Experimental Results

A comparison of the model prediction to the experimental results from Kotagiri et al. (15) and Duan et al. (23) is shown in Figure 3B (23). Kotagiri et al. (15) used 25-nm TiO$_2$ nanoparticles (concentration, 2.5 µg/mL) and 4 different radioactivity levels (31.45, 14.80, 7.40, and 0.37 MBq) (Fig. 3A). Duan et al. (23) used ≈30-nm TiO$_2$ nanoparticles (concentration, 100 µg/mL) and 14.8, 7.4, and 3.7 MBq of ^{18}F-FDG. Experimental results in both studies revealed that tumor cell viability (percentage of control) was a function of ^{18}F-FDG dose (Figs. 3a and 3b in Kotagiri et al. (15) and Fig. 4b in Duan et al. (23)). Fractional decreases in tumor
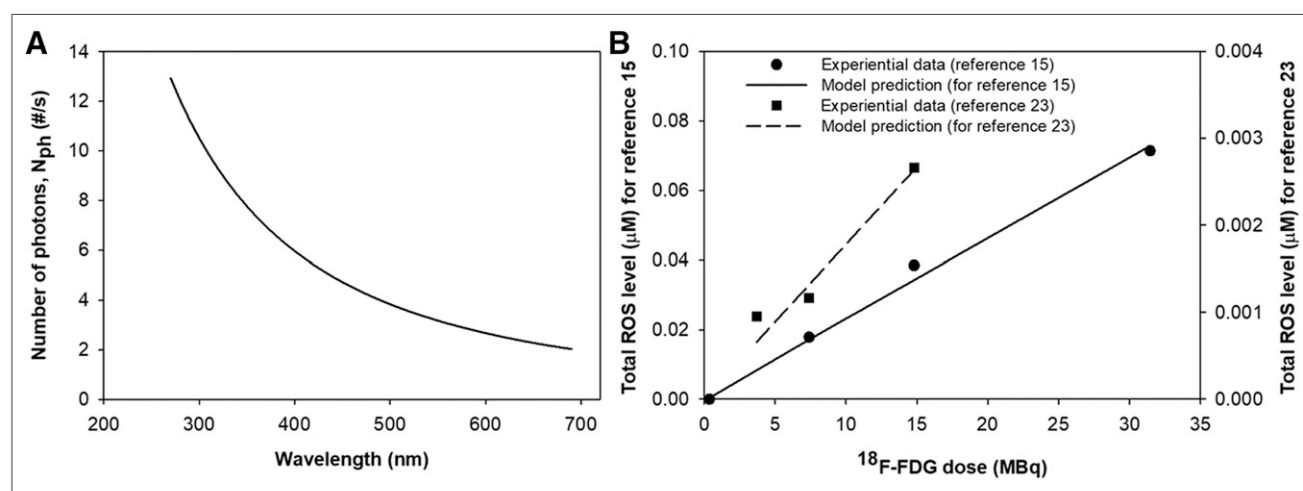

FIGURE 3. (A) Number of Cerenkov photons generated as function of wavelength. (B) Comparison of model predictions to experimental results reported by Kotagiri et al. (15) and Duan et al. (23). Parameters (d_p, C_{TiO_2}, and A) taken from those studies were used to determine equivalent ROS concentration from model. # = numbers.
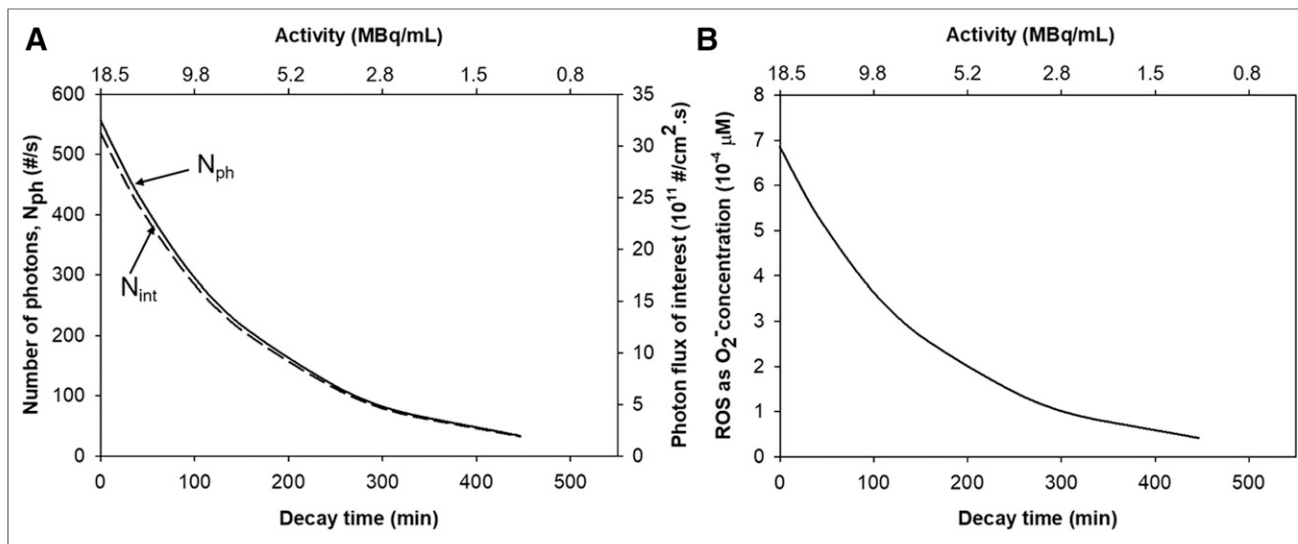
FIGURE 4. Effect of decay time (and radioactivity of ^{18}F-FDG) on N_{ph} (solid curve) and N_{int} (broken curve) (A) and on ROS concentration (B). # = numbers.

cell viability were then converted into equivalent intracellular ROS generation using a constant scaling factor (different scaling factors in the 2 studies but the same scaling factor for all data points in a particular study). For validation of the model, the experimental parameters mentioned earlier were used to calculate the ROS concentration from the model. ROS production predicted from the model (solid line, Fig. 3B) agreed well with the experimental data (solid symbols, Fig. 3B) from both studies.

Effect of Radioactivity (or Decay Time)

The effect of radioactivity was similar to the effect of decay time according to the following formula:

$$A = A_0 \exp(-\lambda' t), \lambda' = \frac{\ln 2}{t_{1/2}}. \qquad \text{Eq. 15}$$

Here, A_0 is the initial activity of the radionuclide, A is the activity at any time t, λ' is the decay constant, and $t_{1/2}$ is the half-life. The radioactivity decreased exponentially with time; therefore, if the TiO$_2$ nanoparticle size was kept constant at 10

nm and the TiO$_2$ concentration was kept constant at 2.5 μg/mL, the number of photons and photon flux (Fig. 4A) and the ROS concentration (Fig. 4B) also decreased exponentially with decay time.

Effect of TiO$_2$ Concentration

The effect of TiO$_2$ concentration was investigated (Fig. 5) by keeping the d_p constant at 10 nm and A at 7.4 MBq/mL. As the C_{TiO_2} increased, the number of TiO$_2$ nanoparticles (N_{TiO_2}) increased and x_{avg} decreased. The important parameters were lengths l_{OA} and l_{AB} (Eq. 5). An increase in the concentration led to a decrease in l_{OA}, whereas l_{AB} remained constant. The smaller the l_{OA}, the smaller the energy loss of the β-particle before the production of photons in the l_{AB} range. Hence, at higher C_{TiO_2}, high-energy β-particles produced more photons, whereas at lower C_{TiO_2}, low-energy β-particles produced fewer photons over the same l_{AB} range.

The photon flux followed a trend similar to that of the number of photons because of the constant size of the TiO$_2$ nanoparticles. Overall, both N_{ph} and N_{int} increased with an increase in concentration
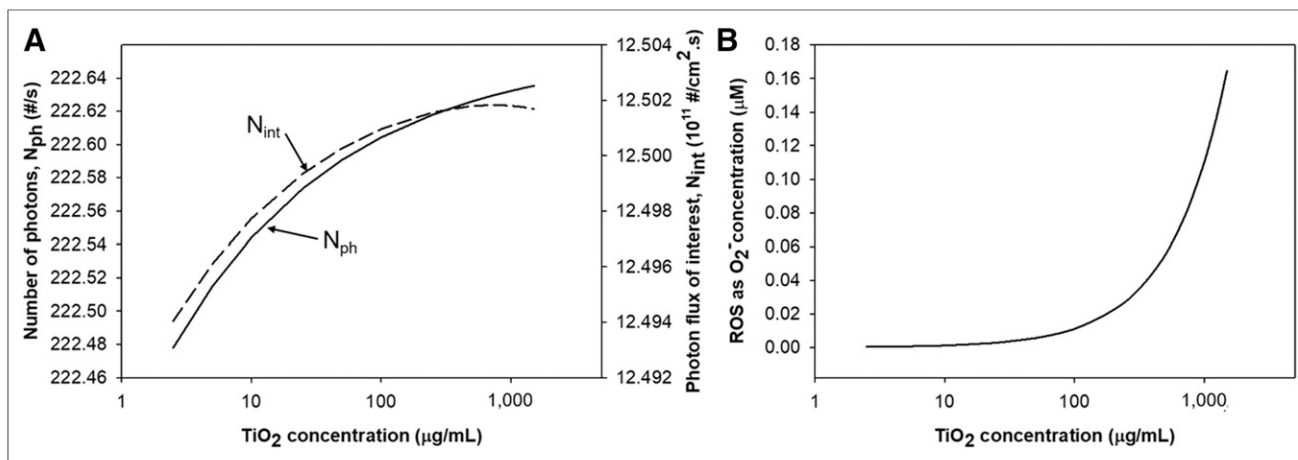

FIGURE 5. Effect of TiO$_2$ concentration on N_{ph} (solid curve) and N_{int} (broken curve) (A) and on ROS concentration (B). # = numbers.

(Fig. 5A). Additionally, more TiO$_2$ nanoparticles were present to absorb CR, increasing the ROS yield (Fig. 5B). Mathematically, according to Equation 14, the ROS concentration was proportional to the number of TiO$_2$ nanoparticles and the square root of the photon flux; hence, ROS production rose with C_{TiO_2}.

Effect of TiO$_2$ Nanoparticle Size

Figure 6A shows the effect of nanoparticle size (d_p) on N_{ph} and N_{int}. C_{TiO_2} and A were kept constant at 2.5 µg/mL and 7.4 MBq/mL, respectively. As the size increased, N_{TiO_2} decreased and x_{avg} increased. Therefore, the larger the l_{AB}, the larger the number of Cerenkov photons. If l_{OA} were larger, then the l_{AB} segment would appear at a greater distance from the origin of the β-particle, so the β-particle would have less energy in the l_{AB} range and hence would produce fewer photons. According to Equation 5, as d_p increased, l_{AB} increased by a larger extent than l_{OA}; hence, N_{ph} increased, but N_{int} decreased because of its inverse relationship with d_p (Eq. 8).

Interestingly, the effect on ROS concentration was not monotonous (Fig. 6B); the ROS concentration first increased with d_p, peaked at about 800 nm, and then decreased. According to Equation 14, the ROS concentration was directly proportional to d_p, N_{int}, N_{TiO_2}, and absorption efficiency (α'). With an increase in d_p, N_{int} and N_{TiO_2} both decreased, as mentioned earlier, but did not play a significant role compared with the size-dependent optical (absorption and scattering) and electrical properties of the TiO$_2$ nanoparticles. The absorption efficiency of the nanoparticles increased with the size. Conversely, the separation between e^- and h^+ was efficient at smaller sizes, leading to favorable charge carrier dynamics. Therefore, the optical and electrical properties of TiO$_2$ (photoexcitation and e^-–h^+ generation) dominated at particle sizes of less than 800 nm, resulting in considerable e^- and h^+ generation and less recombination. However, with increasing sizes, the properties of the TiO$_2$ nanoparticles became similar to those of the bulk TiO$_2$; that is, the recombination of the charge carrier became much easier, and the photoactivity thus was dominated by the available specific surface area of the particles (21).

DISCUSSION

The CR spectrum from the model followed the Frank–Tamm equation (number of photons α $1/\lambda^2$), and the number of photons generated also matched that in a previous report (28). The model was compared with 2 different experimental studies (15,23). The experiments revealed a change in tumor cell viability as a function of the ^{18}F-FDG dose; this change was then converted into the ROS concentration using a constant scaling factor, and this ROS concentration was compared with the ROS concentration predicted from the model using the experimental parameters from those studies. The scaling factor was needed because the studies did not provide the amount of ROS generation; however, the decrease in cell viability is directly correlated to the ROS production. Additionally, although the scaling factors in the 2 studies were different because of the use of different types of TiO$_2$ nanoparticles and cell lines, the same scaling factor was used for all of the data points in a particular study. The model predictions agreed well with the experimental data from both studies and revealed similar trends, thus indicating the robustness of the model. The ROS concentrations in the 2 studies could not be cross-compared because of the different types of TiO$_2$ nanoparticles used in those studies and their distinct optoelectronic properties. A comparison to additional data would further enhance the validity of the model; however, because of the novel and innovative nature of this methodology, not many studies have reported such data.

Having validated the model, we tested its capabilities in a series of design simulations to illustrate its potential use in guiding PDT. The effects of radionuclide dose (A), TiO$_2$ concentration (C_{TiO_2}), and size (d_p) on the amount of ROS generation were studied. N_{ph} generation and ROS concentration rose with A. This feature will provide guidance on the dose of a radionuclide and the time interval of injection for continued therapeutic effects. C_{TiO_2} also directly affected ROS production. The higher the concentration, the larger the N_{ph} and the N_{int}. Furthermore, more TiO$_2$ nanoparticles were present to absorb the photons; therefore, more ROS was produced at a higher TiO$_2$ concentration. The upper limit of the concentration was ultimately constrained by the distance between the β-particles and TiO$_2$, which tended toward zero at very high C_{TiO_2}, and the cytotoxicity of the TiO$_2$ particles. There has been only 1 study (16) on the effect of photocatalyst concentration on cancer cell viability. In that study, cell viability was reported to decrease (as ROS concentration increased) linearly with an increase in the photocatalyst concentration, supporting the model predictions.
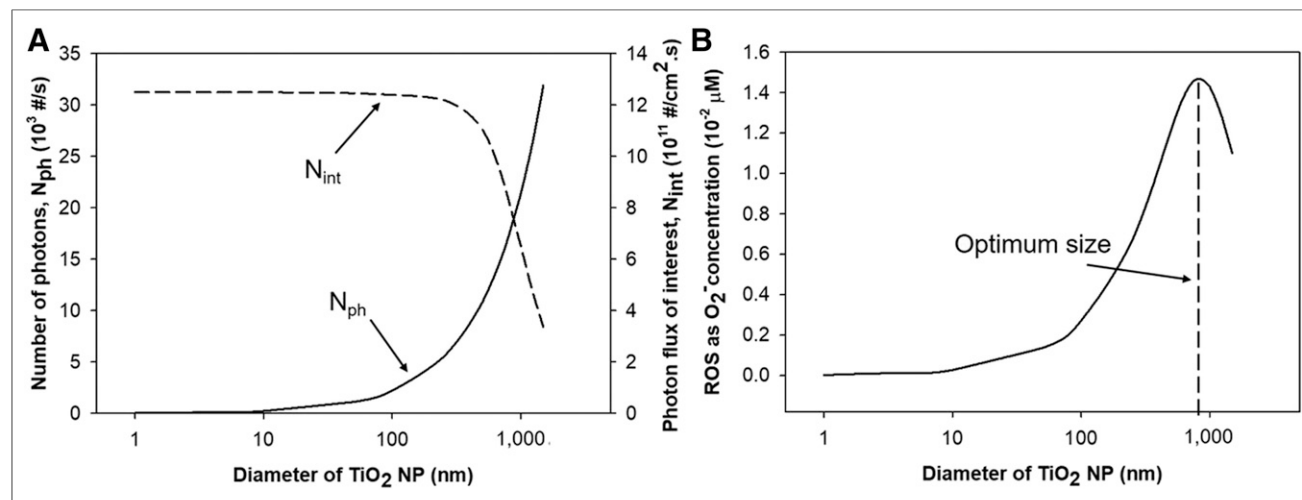

FIGURE 6. Effect of TiO$_2$ nanoparticle (NP) size on N_{ph} (solid curve) and N_{int} (broken curve) (A) and on ROS concentration (B). # = numbers.

The effect of d_p was not monotonous. Although N_{int} decreased with an increase in d_p, the amount of ROS increased at smaller particle sizes, peaked at about 800 nm, and then decreased. Therefore, there is an optimum size of TiO_2 particles for producing the highest ROS concentration. However, the optimal size of 800 nm observed in the model might not be practical for delivering particles to a tumor. Therefore, a balance should be sought by decreasing the size and increasing the concentration of TiO_2 particles. Until now, there has been no study on the effect of the size of TiO_2 nanoparticles on the number of Cerenkov photons and cancer cell viability (ROS production). However, the size of nanoparticles is an important parameter and affects their reactivity, as shown in the literature as well (21,38).

The model can be used easily for any kind of nanoparticle and radionuclide to determine the CR-assisted production of ROS. There are 4 other important points to consider for future work. First, the refractive index of the medium changes with the addition of a radionuclide and nanoparticles, and there is no direct formula to account for the change. A higher refractive index decreases the threshold energy for β-particles to produce CR and, therefore, more photons are generated. Second, the mechanism of ROS generation is complex. Because the present study is the first—to our knowledge—to show a detailed pathway of cancer cell death caused by radionuclides and semiconductor nanoparticles, we described a simple reaction mechanism for ROS generation. However, other complex reaction and ROS products (H_2O_2 and singlet oxygen) have been reported in the literature (36,37). Third, more experimental investigation is needed to provide data for continued model validation. Fourth, the presence of other mechanisms, such as direct excitation and ionization of nanoparticles by ionizing radiation, may also contribute to ROS generation, as reported in previous studies (24,39). Direct excitation of nanoparticles was demonstrated by measuring the radiance output of nanoparticles in the presence of radionuclides that emitted β-particles with less energy than the Cerenkov threshold. The enhancement of the emitted radiance output compared with that in the system without nanoparticles implied the direct excitation of nanoparticles with ionizing radiation. Ionization of nanoparticles by ionizing radiation was determined by measuring the characteristic x-rays produced during ionization (24). For a system of ^{18}F-FDG radionuclides with activity (<30 MBq) that emits mainly the β$^+$ and TiO_2 nanoparticles considered in the present work, these mechanisms play small roles. However, they are significant when the radioactivity is high and when nanoparticles with high-atomic-number elements (e.g., Eu_2O_3, Gd_2O_3) are used.

To the best of our knowledge, there has not been any study on the theoretic determination of the contributions of these mechanisms to ROS generation. It will be of interest to determine the contribution of each individual mechanism to ROS generation and PDT; such a determination was beyond the scope of the present study. However, the model described in the present study still quantifies the contribution of CR to ROS generation and provides a fair idea about the size and concentration of TiO_2 nanoparticles to be used for the effective suppression of cancer cells. Nonetheless, it is also important to experimentally measure ROS generation in this kind of system. The consideration of other mechanisms (described earlier) will affect the scaling factor used to compare the model prediction of the ROS level with the experimental results, and the scaling factor will change because the model will then include ROS generated from these mechanisms.

CONCLUSION

We integrated Cerenkov physics, light scattering, and photocatalytic reaction engineering to understand the detailed mechanism of ROS production (directly attributed to cell death) in the presence of radionuclides and TiO_2 semiconductor nanoparticles. CR is produced when a β-particle (the decay product of a radionuclide) moves at a very high speed in the medium. CR, which is dominant in the UV region, is absorbed by the locally present photoactive TiO_2 nanoparticles—resulting in the generation of e^- and h^+ pairs. The charge carriers then react with the medium and produce ROS, which result in cell death. Furthermore, different system parameters (size of TiO_2 nanoparticles, concentration of TiO_2, and radioactivity of the nuclide) influence the number of Cerenkov photons and ROS generation. The results suggested an optimum TiO_2 particle size for maximum ROS production as a result of the dependence of light absorption, scattering efficiencies, and charge separation on the particle size. These models can also be used for other types of radionuclide and semiconducting materials and can provide a framework for developing and deploying cancerous tumor–mitigating strategies.

REFERENCES

1. Thorek DL, Robertson R, Bacchus WA, et al. Cerenkov imaging: a new modality for molecular imaging. *Am J Nucl Med Mol Imaging.* 2012;2:163–173.
2. Mitchell GS, Gill RK, Boucher DL, Li C, Cherry SR. In vivo Cerenkov luminescence imaging: a new tool for molecular imaging. *Philos Trans A Math Phys Eng Sci.* 2011;369:4605–4619.
3. Dothager RS, Goiffon RJ, Jackson E, Harpstrite S, Piwnica-Worms D. Cerenkov radiation energy transfer (CRET) imaging: a novel method for optical imaging of PET isotopes in biological systems. *PLoS One.* 2010;5:e13300.
4. Das S, Haedicke K, Grimm J. Cerenkov-activated sticky tag for in vivo fluorescence imaging. *J Nucl Med.* 2018;59:58–65.
5. D'Souza JW, Hensley H, Doss M, et al. Cerenkov luminescence imaging as a modality to evaluate antibody-based PET radiotracers. *J Nucl Med.* 2017;58:175–180.
6. Shaffer TM, Pratt EC, Grimm J. Utilizing the power of Cerenkov light with nanotechnology. *Nat Nanotechnol.* 2017;12:106–117.
7. Čerenkov PA. Visible radiation produced by electrons moving in a medium with velocities exceeding that of light. *Phys Rev.* 1937;52:378.
8. Jelley J. Cerenkov radiation and its applications. *British Journal of Applied Physics.* 1955;6:227–232.
9. Collins GB, Reiling VG. Čerenkov radiation. *Phys Rev.* 1938;54:499.
10. Thorek DL, Das S, Grimm J. Molecular imaging using nanoparticle quenchers of Cerenkov luminescence. *Small.* 2014;10:3729–3734.
11. Kotagiri N, Niedzwiedzki DM, Ohara MK, Achilefu S. Activatable probes based on Cerenkov radiation-associated distance dependent luminescence. *Angew Chem Int Ed Engl.* 2013;52:7756–7760.
12. Thorek DL, Ogirala A, Beattie BJ, Grimm J. Quantitative imaging of disease signatures through radioactive decay signal conversion. *Nat Med.* 2013;19:1345–1350.
13. Hu Z, Qu Y, Wang K, et al. In vivo nanoparticle-mediated radiopharmaceutical-excited fluorescence molecular imaging. *Nat Commun.* 2015;6:7560.

14. Ran C, Zhang Z, Hooker J, Moore A. In vivo photoactivation without "light": use of Cherenkov radiation to overcome the penetration limit of light. *Mol Imaging Biol.* 2012;14:156–162.

15. Kotagiri N, Sudlow GP, Akers WJ, Achilefu S. Breaking the depth dependency of phototherapy with Cerenkov radiation and low-radiance-responsive nanophotosensitizers. *Nat Nanotechnol.* 2015;10:370–379.

16. Kamkaew A, Cheng L, Goel S, et al. Cerenkov radiation induced photodynamic therapy using chlorin e6-loaded hollow mesoporous silica nanoparticles. *ACS Appl Mater Interfaces.* 2016;8:26630–26637.

17. Kavadiya S, Chadha TS, Liu H, Shah VB, Blankenship RE, Biswas P. Directed assembly of the thylakoid membrane on nanostructured TiO_2 for a photo-electrochemical cell. *Nanoscale.* 2016;8:1868–1872.

18. de Carvalho BA, Kavadiya S, Huang S, Niedzwiedzki DM, Biswas P. Highly stable perovskite solar cells fabricated under humid ambient conditions. *IEEE Journal of Photovoltaics.* 2017;7:532–538.

19. Kavadiya S, Niedzwiedzki DM, Huang S, Biswas P. Electrospray-assisted fabrication of moisture-resistant and highly stable perovskite solar cells at ambient conditions. *Advanced Energy Materials.* 2017. https://doi.org/10.1002/aenm.201700210. Accessed November 19, 2018.

20. Lin L-Y, Nie Y, Kavadiya S, Soundappan T, Biswas P. N-doped reduced graphene oxide promoted nano TiO_2 as a bifunctional adsorbent/photocatalyst for CO_2 photoreduction: effect of N species. *Chem Eng J.* 2017;316:449–460.

21. Almquist CB, Biswas P. Role of synthesis method and particle size of nanostructured TiO_2 on its photoactivity. *J Catal.* 2002;212:145–156.

22. Namkhang P, An W-J, Wang W-N, Rane KS, Kongkachuichay P, Biswas P. Low temperature synthesis of N-doped TiO_2 nanocatalysts for photodegradation of methyl orange. *J Nanosci Nanotechnol.* 2013;13:2376–2381.

23. Duan D, Liu H, Xu Y, et al. Activating TiO_2 nanoparticles: gallium-68 serves as a high-yield photon emitter for Cerenkov-induced photodynamic therapy. *ACS Appl Mater Interfaces.* 2018;10:5278–5286.

24. Pratt EC, Shaffer TM, Zhang Q, Drain CM, Grimm J. Nanoparticles as multimodal photon transducers of ionizing radiation. *Nat Nanotechnol.* 2018;13:418–426.

25. Zhou Z, Song J, Nie L, Chen X. Reactive oxygen species generating systems meeting challenges of photodynamic cancer therapy. *Chem Soc Rev.* 2016;45:6597–6626.

26. Glaser AK, Zhang R, Gladstone DJ, Pogue BW. Optical dosimetry of radiotherapy beams using Cherenkov radiation: the relationship between light emission and dose. *Phys Med Biol.* 2014;59:3789–3811.

27. Glaser AK, Zhang R, Andreozzi JM, Gladstone DJ, Pogue BW. Cherenkov radiation fluence estimates in tissue for molecular imaging and therapy applications. *Phys Med Biol.* 2015;60:6701.

28. Gill RK, Mitchell GS, Cherry SR. Computed Cerenkov luminescence yields for radionuclides used in biology and medicine. *Phys Med Biol.* 2015;60:4263–4280.

29. Beattie BJ, Thorek DL, Schmidtlein CR, Pentlow KS, Humm JL, Hielscher AH. Quantitative modeling of Cerenkov light production efficiency from medical radionuclides. *PLoS One.* 2012;7:e31402.

30. Ouyang Z, Liu B, Yasmin-Karim S, Sajo E, Ngwa W. Nanoparticle-aided external beam radiotherapy leveraging the Čerenkov effect. *Phys Med.* 2016;32:944–947.

31. Almquist CB, Biswas P. A mechanistic approach to modeling the effect of dissolved oxygen in photo-oxidation reactions on titanium dioxide in aqueous systems. *Chem Eng Sci.* 2001;56:3421–3430.

32. Kotagiri N, Laforest R, Achilefu S. Reply to 'Is Cherenkov luminescence bright enough for photodynamic therapy?'. *Nat Nanotechnol.* 2018;13:354–355.

33. Anderson W, Belcher E. A standard light source of very low intensity based on the Cerenkov effect. *British Journal of Applied Physics.* 1954;5:53–57.

34. National Institute of Standards and Technology. ESTAR stopping-power and range tables for electrons. https://physics.nist.gov/PhysRefData/Star/Text/ESTAR.html. Accessed November 19, 2018.

35. Physical Sciences Resource Center. Lund/LBNL nuclear data search. https://psrc.aapt.org/items/detail.cfm?ID=258. Accessed November 19, 2018.

36. Villarreal TL, Gómez R, Gonzalez M, Salvador P. A kinetic model for distinguishing between direct and indirect interfacial hole transfer in the heterogeneous photooxidation of dissolved organics on TiO_2 nanoparticle suspensions. *J Phys Chem B.* 2004;108:20278–20290.

37. Gerischer H, Heller A. The role of oxygen in photooxidation of organic molecules on semiconductor particles. *J Phys Chem.* 1991;95:5261–5267.

38. Jiang J, Oberdörster G, Elder A, Gelein R, Mercer P, Biswas P. Does nanoparticle activity depend upon size and crystal phase? *Nanotoxicology.* 2008;2:33–42.

39. Niu G, Chen X. When radionuclides meet nanoparticles. *Nat Nanotechnol.* 2018;13:359–360.

Errata

In the article "^{18}F-Flortaucipir PET/MRI Correlations in Nonamnestic and Amnestic Variants of Alzheimer Disease," by Nasrallah et al. (*J Nucl Med.* 2018;59:299–306), grant numbers were inadvertently left out of the Disclosure section. The Disclosure should have included the following: The study was also partially funded by NIH grant numbers P01 AG017586 (PI. Virginia M. Lee), P30-AG010124 (PI. John Q. Trojanowski), and AG054519 (PI. Murray Grossman). The authors regret the error.

In the article "Immediate Postablation ^{18}F-FDG Injection and Corresponding SUV Are Surrogate Biomarkers of Local Tumor Progression After Thermal Ablation of Colorectal Carcinoma Liver Metastases," by Cornelis et al. (*J Nucl Med.* 2018;59:1360–1365), values in the SUV_{mean} and SUV_{max} columns of Table 1 were reversed. The corrected table appears below. The authors regret the error.

TABLE 1
Average SUVs of ROIs Before and After Ablation

ROI	SUV_{mean}	SUV_{max}
Including tumors		
Before ablation	2 (0.6)	9.2 (6.2)
After ablation	2.2 (0.6)	4.5 (1.7)
Including liver background only		
Before ablation	2.5 (0.5)	3.8 (1.6)
After ablation	3.2 (0.6)	4 (0.9)